Electromechanical Impedance Method for the Health Monitoring of Bonded Joints: Numerical Modelling and Experimental Validation

Vincenzo Gulizzi[1,2], Piervincenzo Rizzo[2,3] and Alberto Milazzo[4]

Abstract: The electromechanical impedance (EMI) method is one of the many nondestructive evaluation approaches proposed for the health monitoring of aerospace, civil, and mechanical structures. The method consists of attaching or embedding one or more wafer-type piezoelectric transducers (PZTs) to the system of interest, the host structure, and measuring certain electrical characteristics of the transducers. As these characteristics are also related to the impedance of the host structure, they can be used to infer the mechanical properties of the monitored structure. In the study presented in this paper, we utilize the EMI to monitor the quality of adhesively bonded joints. A finite element formulation was implemented to predict the electromechanical response of PZT attached to simple adhesively-bonded joints. The model was coded in Matlab and its results were validated by comparing them with the results associated with a few case studies implemented using commercial software. The finite element code was used to model the EMI measurement of a simple adhesively bonded joint subjected to adhesive layers of different qualities. Finally, the EMI was validated experimentally. A low cost circuit was designed and assembled to measure the electromechanical characteristics of a PZT glued to the structure of interest. We monitored the curing process of the adhesive forming the joint. This simulates at large the inverse of the degradation that may occur in bonded joints. The experimental results show that the EMI technique is able to capture variations of the stiffness of the adhesive layer.

Keywords: Electromechanical impedance method, bonded joints, structural health

[1] PhD Student, Department of Civil, Environmental, Aerospace, and Materials Engineering. University of Palermo, Viale delle Scienze, Ed. 8, Palermo, 90128, Italy.

[2] Associate Professor, Laboratory for nondestructive evaluation and structural health monitoring studies, Department of Civil and Environmental Engineering. University of Pittsburgh, 3700 O'Hara Street, Pittsburgh, PA, 15261, USA.

[3] Corresponding author: Tel. +1-412-624-9575; Fax: +1-412-624-0135; E-mail: pir3@pitt.edu

[4] Associate Professor, Department of Civil, Environmental, Aerospace, and Materials Engineering. University of Palermo, Viale delle Scienze, Ed. 8, Palermo, 90128, Italy.

monitoring, finite element method.

1   Introduction

The use of low-weight, robust and fatigue-resistant adhesive joints in lieu of fastened joints has found application in air, ground and sea vehicles for both commercial and military use. In aeronautical structures, adhesive joints are mainly used to connect stringers and skin for wings and fuselage as well as for junctions of the empennage, elevators, tabs and spoilers [Baker and Jones (1988); Higgins (2000); Baker et al. (2003)]. There are three mechanisms that may lead a bonded joint to failure: presence of voids or disbond, poor cohesive strength and poor adhesive strength [Guyott et al. (1986)]. Cohesive failure is characterized by the presence of the adhesive on the bonded surfaces and it is usually the result of poor joint design, such as insufficient overlap length, high peel stresses and/or excessive porosity, due to exposure of the uncured adhesive to humidity. Adhesion failure is instead characterized by the clear absence of the adhesive on one of the bonded surface and it is usually due to an inappropriate surface preparation and/or a late application of the adhesive. Bond degradation, if left undetected, can lead to reduced vehicle readiness and increased total ownership costs. The quality assessment of adhesively-bonded components represents a long-standing challenge in the field of nondestructive evaluation (NDE). Methods based on the use of ultrasounds [Guyott and Cawley (1988); Nagy (1991); Nagy (1992); Lowe et al. (2000); Rothenfusser et al. (2000); Yan et al. (2009)], pulse thermography [Schroeder et al. (2002); Waugh et al. (2011)] and digital image correlation [Vijaya Kumar et al. (2013)] were investigated. In particular, the application of guided ultrasonic waves [Lanza di Scalea et al. (2004a, 2004b); Matt et al. (2005); Todd et al. (2010)] is feasible for the health monitoring of the joints.

In the study presented in this paper, we utilize the electromechanical impedance (EMI) method for the structural health monitoring (SHM) of adhesively bonded components. The objective is to explore the feasibility of the EMI method at capturing bond degradation, i.e. poor bond strength. In general, the method consists of bonding or embedding one or more wafer-type lead zirconate titanate (PZT) transducers, hereafter indicates as PZTs, to the material, the host structure, to be monitored. When subjected to an electric field, the transducer induces low to high frequency structural excitations which, in turn, affect the transducers electrical admittance. Since the structural vibrations depend on the mechanical impedance of the host structure, the measurement of the PZT's conductance and susceptance can be exploited to infer the health of the host element [Park et al. (2003); Peairs et al. (2004); Tabrizi et al. (2012)]. The advantages of EMI-based SHM include: low-cost, lightweight and sensitivity to stiffness or mass changes in the area near the

PZT. The interested reader is referred to Park et al. (2003) and Park et al. (2007) for a complete review of the method.

As discussed in the next section the EMI method was applied to many engineering systems for SHM purposes. However, its application to bonded elements is limited to the experimental works of Na et al. (2012) and Malinowski et al. (2014). Na et al. considered the health monitoring of an adhesively bonded lap joint in a corrosive environment. They used small and short adhesively bonded joints subjected to a corrosive environment to develop a reusable wafer-type sensor. The work, exclusively experimental, was conducted using an AD5933 evaluation board, discussed in section 5. Malinowski et al (2014) employed the EMI to characterize composites elements with different adhesive bonds. Samples of the same joint were built with different types of inclusion (agent contamination, moisture contamination and poor curing) at each joint. A PZT was glued at the middle of each specimen and the electromechanical response was measured with an impedance analyzer at a frequency range containing the natural modes of vibration of the PZT.

In our study, we first implemented an *in house* finite element (FE) model to predict the behavior of a PZT attached to a host structure. To the best of our knowledge, this is the first time that the EMI method was simulated not using a commercial software. The model was first validated by comparing its results with a FE-based EMI simulation reported in literature [Bhalla et al. (2012)] and obtained using the commercial software ANSYS. Then, the effect of the modulus and loss factor of the adhesive layer on the admittance of the PZT was quantified. Finally, the model was validated experimentally by monitoring simple aluminum plates stiffened by means of an aluminum strip. The inverse process of bond degradation was simulated at large by observing the effect of curing on the electrical properties of a PZT glued to the plate.

2 Background on EMI

The EMI method exploits the coupling between the electromechanical properties of a piezoelectric material and the mechanical properties of the host structure to which the material is bonded or embedded. By using an external voltage $v(t) = Ve^{j\omega t}$, a patch made of a piezoelectric material is excited at different frequencies. The electromechanical coupling induces a displacement filed at both the patch and the structure. The response of the whole system is measured in terms of the current $i(t) = I(\omega)e^{j\omega t}$ flowing in a circuit connected to the patch and in terms of the admittance $Y(\omega) = I(\omega)/V$. The admittance $Y(\omega)$ is a complex quantity consisting of a real part, the conductance $G(\omega)$, and an imaginary part, the susceptance $B(\omega)$. The plot of $G(\omega)$ and $B(\omega)$ as a function of the actuation frequency represents a unique signature for the structure, and may serve for its diagnosis. In fact, these

plots present peaks corresponding to the structural vibration modes, which identify the mechanical impedance of the structure within the sensing region of the PZT. The underlying hypothesis of any EMI-based SHM is that any change in the properties (mass, stiffness, damping, integrity, etc...) of the structure affects this signature. For illustrative purposes, Fig. 1 shows the signature, i.e. the conductance as a function of the actuation frequency, of one of the PZTs used in the experiments. The plot refers to free boundary conditions. The peaks at 170 kHz, 245 kHz and 440 kHz represent the resonant mode of vibration of the transducer within the 100-500 kHz interval.
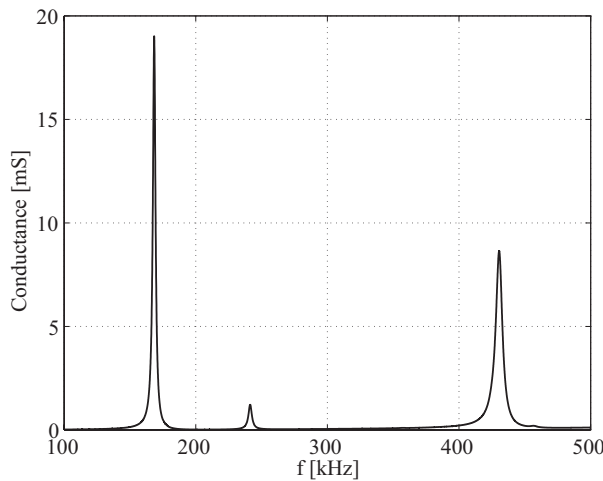
Figure 1: Conductance as a function of the actuation frequency of a free PZT.

The use of the EMI technique has emerged as an effective tool for the health monitoring of structures [Park et al. (2003); Bhalla et al. (2012); Ayres et al. (1998); Soh et al. (2000); Park et al. (2001); Giurgiutiu and Zagrai, (2002)]. Besides the static approach [Crawley and De Luis (1987)] different models of the PZT-structure dynamic interaction were proposed to describe the basic principles. Liang et al [Liang et al. (1994)] developed a one-degree-of-freedom model of such interaction in which the piezoelectric device is modeled as a thin bar of length l, width w and thickness h, connected to the host structure that is represented by an external impedance Z. They showed that the admittance of the sensor-structure system has the following expression:

$$Y(\omega) = j\omega \frac{wl}{h}\left[\bar{\kappa}_{33}^{\varepsilon} + \frac{e_{31}^2}{\bar{c}_{11}^E}\frac{Z_a}{Z+Z_a}\frac{\tan(\xi l)}{\xi l}\right] \qquad (1)$$

where Z and Z_a represent the mechanical impedances of the host structure and the piezoelectric device, respectively; the mechanical impedance Z of a point on a structure is the ratio of the force applied at a point to the resulting velocity at that point. In Eq. (1), $\xi = \omega \sqrt{\rho / \bar{c}_{11}^E}$ is the wavenumber; ρ, $\bar{\kappa}_{33}^\varepsilon$ and $\bar{c}_{11}^E$ are the density, the complex dielectric constant at constant strain and complex stiffness coefficient of the piezoelectric material, respectively. Zhou et al. (1995) extended the one-dimensional interaction to model a two-dimensional piezoelectric patch bonded to a two-dimensional host structure, Bhalla and Soh (2004) proposed a two-dimensional model based on the effective mechanical impedance, while Annamdas and Soh (2007) introduced a three-dimensional approach.

3 Finite element modeling

The use of finite elements was proposed to model piezoelectric both for ultrasonic [Allik and Hughes (1970); Allik et al. (1974); Lerch, (1990)] and smart material [Crawley (1994)] applications. The commercial finite element software ANSYS was used to model the electromechanical impedance method by Park et al. (2006), Liu and Giurgiutiu, (2007), Zhang et al. (2011), Bhalla et al. (2012), Moharana and Bhalla (2012). In particular, Park et al. (2006) modeled piezoelectric sensor on a concrete beam with multiple cracks; Liu and Giurgiutiu, (2007) showed the need for coupled-field elements to model the sensor-host structure interaction; Zhang et al. (2011) compared the response of a piezoelectric sensor bonded to a cracked beam obtained by using a 3D ANSYS analysis with those obtained by using Timoshenko theory; the study of Bhalla et al. (2012) will be detailed later in this paper; Moharana and Bhalla (2012) studied the inclusion of the shear lag effect in the finite element formulation for the EMI.

In the study presented in this paper a time-harmonic fully coupled-field finite element formulation was employed to model the electromechanical impedance technique. For a piezoelectric solid occupying the domain Ω with boundary Γ, the governing equations are obtained by the extended Hamilton's principle expressed in terms of the displacement vector u and the electric potential ϕ [Tiersten (1967)]:

$$\delta \int_{t_0}^{t_1} [T - H + W] dt = 0 \tag{2}$$

where t is the time and T, H and W are the kinetic energy, the electric enthalpy and the external work defined as:

$$T = \int_\Omega \frac{1}{2} \rho \, \dot{\mathbf{u}}^T \dot{\mathbf{u}} d\Omega \tag{3a}$$

$$H = \int_{\Omega} \left(\frac{1}{2} \boldsymbol{\varepsilon}^T \mathbf{c}^E \boldsymbol{\varepsilon} - \mathbf{E}^T \boldsymbol{e} \boldsymbol{\varepsilon} - \frac{1}{2} \mathbf{E}^T \boldsymbol{\kappa}^{\varepsilon} \mathbf{E} \right) d\Omega \tag{3b}$$

$$W = \int_{\Omega} \left(\mathbf{b}^T \mathbf{u} - \rho_e \phi \right) d\Omega + \int_{\Gamma} \bar{\mathbf{t}}^T \mathbf{u} d\Gamma - \int_{\Gamma} \sigma_e \phi d\Gamma \tag{3c}$$

In Eqs. 3, $\mathbf{b}$, ρ and ρ_e are the body forces, the mass density and the body free charge density, respectively; $\underline{t}$ are the prescribed tractions and $\underline{\sigma}_e$ is the prescribed free surface density charge; $\mathbf{c}^E$, $\mathbf{e}$ and $\boldsymbol{\kappa}^{\varepsilon}$ are the elastic stiffness at constant electric field, the piezoelectric coupling and the dielectric permittivity at constant strain, respectively; $\boldsymbol{\varepsilon}$ and $\mathbf{E}$ are the vectors of the strain components and the electric field, respectively.

Focusing on the time-harmonic case which is relevant for the EMI technique, for a finite element Ω^e the classical elemental approximation for the primary variables is introduced as

$$\mathbf{u}(\mathbf{x},t) = \mathbf{N}^u(\mathbf{x}) \delta^u e^{j\omega t} \tag{4}$$

$$\phi(\mathbf{x},t) = \mathbf{N}^{\varphi}(\mathbf{x}) \delta^{\varphi} e^{j\omega t} \tag{5}$$

where $\mathbf{N}^u(\mathbf{x})$ and $\mathbf{N}^{\phi}(\mathbf{x})$ are suitable shape functions for the displacement field and the electric potential, $\boldsymbol{\delta}^u$ and $\boldsymbol{\delta}^{\phi}$ are the complex vectors containing the values of the element nodal displacement and electric potential amplitudes, respectively, and ω is the circular frequency. By using the kinematical and the electric gradient equations, and by replacing Eqs. 4 and 5 into the Hamilton's principle statements, we find the following elemental equations of motion and charge:

$$\left(\mathbf{k}^{uu} - \omega^2 \mathbf{m} \right) \boldsymbol{\delta}^u - \mathbf{k}^{u\varphi} \boldsymbol{\delta}^{\varphi} = \mathbf{f} \tag{6}$$

$$\left(\mathbf{k}^{u\varphi} \right)^T \boldsymbol{\delta}^u + \mathbf{k}^{\varphi\varphi} \boldsymbol{\delta}^{\varphi} = \mathbf{q} \tag{7}$$

where the definition of the mass matrix $\mathbf{m}$, of the stiffness matrices $\mathbf{k}^{uu}$, $\mathbf{k}^{u\phi}$, $\mathbf{k}^{\phi\phi}$ and the equivalent mechanical forces $\mathbf{f}$ and charges $\mathbf{q}$ can be found in Allik and Hughes (1970).

It is worth noting that piezoelectric materials exhibit losses that need to be considered in order to model their behavior accurately especially in EMI applications. This is accomplished by introducing the mechanical, piezoelectric, and dielectric losses η, γ and χ, respectively, which can be obtained empirically. These coefficients are used to introduce the following complex constitutive matrices able to model the energy losses [Mezheritsky (2004)]

$$\bar{\mathbf{c}}^E = \frac{1}{(1 - j\eta)} \mathbf{c}^E \tag{8}$$

$$\bar{\mathbf{e}} = \mathbf{dc}^E \frac{(1 - j\gamma)}{(1 - j\eta)} \tag{9}$$

$$\bar{\boldsymbol{\kappa}}^\varepsilon = \boldsymbol{\kappa}^\sigma (1 - j\chi) - \mathbf{dc}^E \mathbf{d}^T \frac{(1 - j\gamma)^2}{(1 - j\eta)} \tag{10}$$

where $\mathbf{c}^E$, $\mathbf{d}$, $\boldsymbol{\kappa}^\sigma$ are the elastic compliance at constant electric field, the piezoelectric coupling and the dielectric permittivity at constant stress, respectively.

Once introduced the complex constitutive matrices, Eqs. 6 and 7 still hold and take the material losses into account. It is worth noting that Eqs. 6 and 7 hold also for purely mechanical behavior provided that the appropriate constitutive law is applied (zero piezoelectric coupling coefficients).

By using the standard FEM assembly procedure [Bathe (1996)], the discretized equations for the whole structure are written as:

$$\left(\mathbf{K}^{uu} - \omega^2 \mathbf{M} \right) \boldsymbol{\Delta}^u - \mathbf{K}^{u\varphi} \boldsymbol{\Delta}^\varphi = \mathbf{F} \tag{11}$$

$$\left(\mathbf{K}^{u\phi} \right)^T \boldsymbol{\Delta}^u + \mathbf{K}^{\varphi\varphi} \boldsymbol{\Delta}^\varphi = \mathbf{Q} \tag{12}$$

where $\boldsymbol{\Delta}^u$ and $\boldsymbol{\Delta}^\varphi$ contain the nodal displacements and the electric potentials of the whole structure, respectively. The vectors $\boldsymbol{\Delta}^u$ and $\boldsymbol{\Delta}^\varphi$ are partitioned by collecting the nodal unknowns which are denoted by subscript 1, and the assigned quantities which are denoted by subscript 2. Then, Eqs. 11 and 12 can be rewritten and a condensation procedure [Chen et al. (2012)] is applied to write the equation:

$$\left(K - \omega^2 M \right) \boldsymbol{\Delta}_1^u = F \tag{13}$$

which is solved for the unknown nodal displacements $\boldsymbol{\Delta}_1^u$. Once Eq. 13 is solved, the unknown values of the nodal potential can be calculated and the element nodal displacements $\boldsymbol{\delta}^u$ and $\boldsymbol{\delta}^\varphi$ can be retrieved from the solution. Accordingly, the stresses and the electric displacement are computed by means of the piezoelectric constitutive relationships

$$\boldsymbol{\sigma} = \bar{\mathbf{c}}^E \boldsymbol{\varepsilon} - \bar{\mathbf{e}}^T \mathbf{E} = \bar{\mathbf{c}}^E \mathbf{B}^u \boldsymbol{\delta}^u - \bar{\mathbf{e}}^T \mathbf{B}^\varphi \boldsymbol{\delta}^\varphi \tag{14}$$

$$\mathbf{D} = \bar{\mathbf{e}} \boldsymbol{\varepsilon} + \bar{\boldsymbol{\kappa}}^\varepsilon \mathbf{E} = \bar{\mathbf{e}} \mathbf{B}^u \boldsymbol{\delta}^u + \bar{\boldsymbol{\kappa}}^\varepsilon \mathbf{B}^\varphi \boldsymbol{\delta}^\varphi \tag{15}$$

where $\mathbf{B}^u$ and $\mathbf{B}^\varphi$ are obtained by applying the kinematical and electric gradient operators to the shape functions matrices [Lerch, (1990)].

To apply the finite element to the modelling of the EMI technique, measurement of the current owing through the piezoelectric transducer when excited with a voltage across the electrodes is required. Assuming Γ_{el}^e is the electroded surface of the

finite element and **n** be the corresponding outward unit normal, the electric current $\tilde{i}$ is calculated as

$$\tilde{i} = j\omega \int\limits_{\Gamma^e_{el}} \mathbf{n}^T \mathbf{D} \mathrm{d}\Gamma = j\omega \left[\left(\int\limits_{\Gamma^e_{el}} \mathbf{n}^T \mathbf{e} \mathbf{B}^u \mathrm{d}\Gamma \right) \delta^u + \left(\int\limits_{\Gamma^e_{el}} \mathbf{n}^T \kappa^\varepsilon \mathbf{B}^\varphi d\Gamma \right) \delta^\varphi \right]$$

$$= j\omega \left[\mathbf{\Lambda}^u \delta^u + \mathbf{\Lambda}^\varphi \delta^\varphi \right]$$

(16)

The current owing through the piezoelectric device is then calculated as the sum over all the elements whose surfaces belong to the electrode

$$I(\omega) = \sum \tilde{i}$$

(17)

By taking the ratio between the current calculated $I(\omega)$ and voltage applied V at each frequency of interest, the electrical admittance $Y = I(\omega)/V$ is obtained.

4   Numerical results

The 3-D finite element formulation discussed in the previous Section was implemented in Matlab. A 20-node brick element with four degrees of freedom for each node was used. We first validated and calibrated our model by computing the structural response of a few systems reported in the literature [Bhalla et al. (2012)] and by comparing the results. We analyzed a 10 mm x 10 mm x 0.3 mm square piezoelectric patch freely suspended. The patch was a PIC 151 (PI Ceramics) transducer. Owing to the symmetry of the problem, only a quarter of the patch was modeled. The mesh consisted of one hundred 0.5 mm x 0.5 mm x 0.3 mm elements. The analysis was carried out in the frequency range 100-900 kHz at steps of 100 Hz. Figures 2a and 2b show the conductance and the susceptance signatures of the free PZT. The results are compared with those of Bhalla et al. (2012) and they show an excellent agreement in terms of amplitude and number of peaks.

The PZT-structure interaction presented in Bhalla et al. (2012) was then modelled. The system consisted of the same PIC 151 patch attached to a 231 mm x 21 mm x 2 mm aluminum plate by means of a 0.03 mm bonding layer between the PZT and the plate. The system is shown in Fig. 3a. In our model we considered the X-Y (1-2) plane as the plane of isotropy, in accordance with the specifications of the manufacturer, i.e. we considered the following compliance coefficients: $s_{22} = s_{11} = 15.0*10^{-12}$ [m^2/N]. The conductance signature was calculated in the frequency range from 30 kHz to 60 kHz and a frequency step of 10 Hz was used. Figure 3b compares the conductance calculated in the present study and the conductance obtained in Bhalla et al. (2012). The plot shows that most of the frequencies at which the structural peaks occur are in agreement.
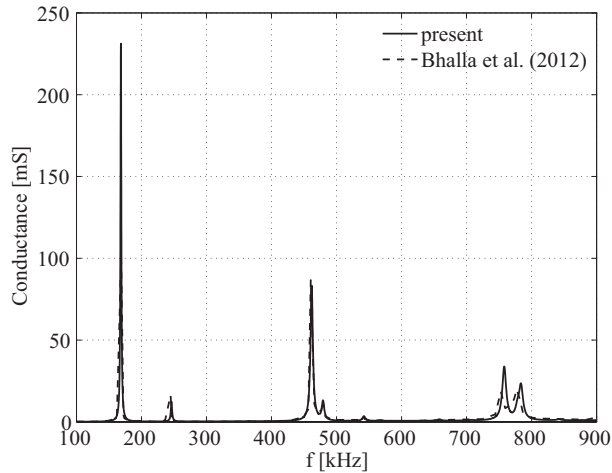
(a)
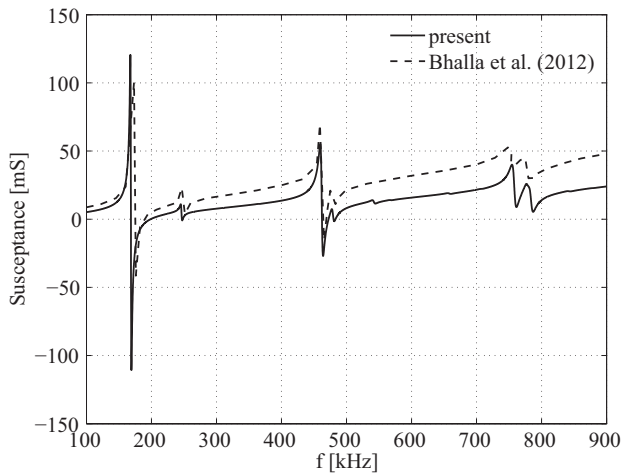
(b)

Figure 2: Finite element modelling of a free PZT. Comparative analysis of the results obtained by using our finite element model and the results obtained by Bhalla et al. (2012) using ANSYS. (a) Conductance and (b) susceptance as a function of the actuation frequency.

(a)

(b)
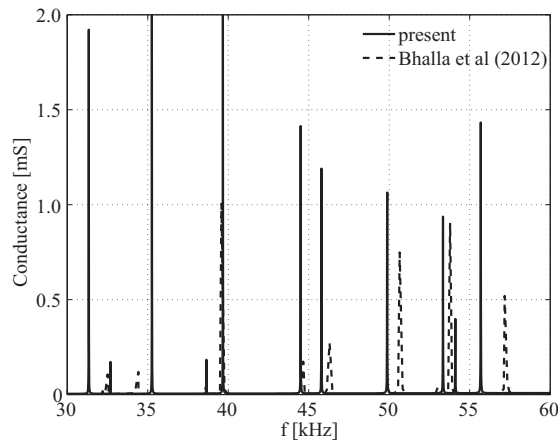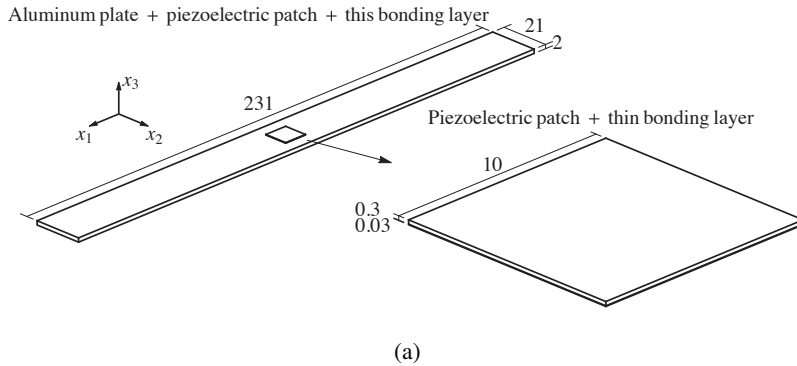
Figure 3: Finite element modelling of a PZT attached to an aluminum plate. (a) Geometry of the system. (b) Conductance as a function of the actuation frequency computed by using our finite element model and obtained by Bhalla et al. (2012) using ANSYS.

Then, we estimated numerically the response of a piezoelectric transducer bonded to a host structure. Two analyses were carried out. First, we calculated the response of the same free PZT used in the experimental study to determine its natural modes of vibration. Second, we computed the response of the same PZT attached to a simple adhesively-bonded joint. The latter system aimed at evaluating the capability of the proposed SHM method at capturing variations of the bond stiffness.

The geometry and the mesh of the free PZT are schematized in Fig. 4a. A 10 mm x 10 mm x 2 mm patch having the same characteristics of PSI-5A4E transducers

(a)

(b)

(c)
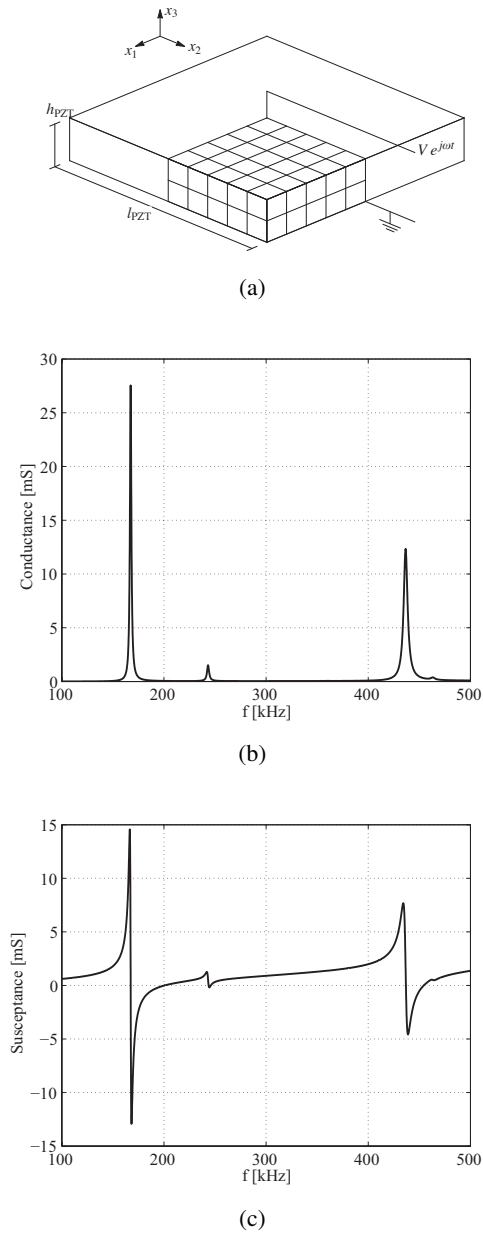
Figure 4: Numerical model of the PSI-5A4E transducer used in the experimental studies. (a) geometry and mesh of a quarter of the transducer. (b) conductance and (c) susceptance signatures of the freely-suspended transducer.

supplied by Piezo System was modeled. The properties of the material are listed in Tab. 1. Owing to the symmetry of the system, only a quarter of the transducer was meshed. The conductance and the susceptance signatures of the free PZT are shown in Figs. 4b and 4c, respectively. The range 100 – 500 kHz was chosen as it includes the first peaks of resonance of the PZT. Two main peaks are clearly visible at 175 kHz and 440 kHz.

Table 1: Properties of the PSI-5A4E transducer used in the present study.

Property	Symbol	Value
Density [kg/m^3]	ρ	$7.8 \cdot 10^3$
Compliance 10^{-12}[m^2/N]	s_{11}^E, s_{22}^E	15.2
	s_{33}^E	19.2
	s_{12}^E	-4.8
	s_{13}^E, s_{23}^E	-5.7
	s_{44}^E, s_{55}^E	47.8
	s_{66}^E	39.9
Piezoelectric coupling 10^{-10}[C/N] or [m/V]	d_{31}, d_{32}	-1.9
	d_{33}	3.9
	d_{15}, d_{24}	5.9
Dielectric permittivity [nF/m]	$\kappa_{11}^\sigma, \kappa_{22}^\sigma$	15.5
	κ_{33}^σ	16.3
Loss factors (100 - 500 kHz)	η	$1.0 \cdot 10^{-2}$
	γ	0.0
	χ	$0.2 \cdot 10^{-1}$
Loss factors (60 - 70 kHz)	η	$2.2 \cdot 10^{-3}$
	γ	0.0
	χ	$0.2 \cdot 10^{-1}$

The same PZT was glued to a 127 mm x 127 mm x 1.27 mm aluminum plate. A 127 mm x 25.4 mm x 1.27 mm aluminum beam, which plays the role of a stiffener, was also bonded above the plate. The mechanical properties of the elements are summarized in Tab. 2, whereas the complete system is shown in Fig. 5a and the principal dimensions are listed in Tab. 3. The properties of the adhesive are those typical of a commercial ambient-cure, Devcon 2 Ton Epoxy type. The plate and the stiffener were meshed as shown in Fig. 5b. Only half of the system was modeled, and the mesh consisted of 4064 elements. The adhesive layer was also modeled with 3D finite elements and it was considered linear elastic. The response in terms of the conductance signature of the PZT was calculated again in the frequency range 60-70 kHz at a frequency step of 10 Hz. The numerical analysis was carried out for

Table 2: Properties of the aluminum plate and stiffener, the bonding layer of the PZT and the structural adhesive to be monitored used in the present study.

Element	Property	Symbol	Value
Aluminum	Density [kg/m^3]	ρ_p	$2.7{\cdot}10^3$
	Young modulus [GPa]	Y_p	68.9
	Poisson ratio	ν_p	0.3
	Mechanical loss factor	η_p	$4.4{\cdot}10^{-4}$
Bonding layer	Density [kg/m^3]	ρ_b	$1.0{\cdot}10^3$
	Young modulus [GPa]	Y_b	1
	Poisson ratio	ν_b	0.4
	Mechanical loss factor	η_b	$0.5{\cdot}10^{-2}$
Structural adhesive	Density [kg/m^3]	ρ_{ad}	$1.0{\cdot}10^3$
	Young modulus [GPa]	Y_{ad}	2.5
	Poisson ratio	ν_{ad}	0.4
	Mechanical loss factor	η_{ad}	$0.5{\cdot}10^{-1}$

Table 3: Geometrical properties of the adhesively-bonded joint system.

Element	Dimension	Value [mm]
plate	width w_p	$1.27{\cdot}10^2$
	length l_p	$1.27{\cdot}10^2$
	thickness h_p	1.27
stiffener	width w_s	$2.54{\cdot}10^1$
	length l_s	$1.27{\cdot}10^2$
	thickness h_s	1.27
adhesive layer	width w_{ad}	$2.54{\cdot}10^1$
	length l_{ad}	$1.27{\cdot}10^2$
	thickness h_{ad}	0.36
PZT	width l_{PZT}	10.00
	length l_{PZT}	10.00
	thickness h_{PZT}	2.00
PZT's bonding layer	width l_b	10.00
	length l_b	10.00
	thickness h_b	0.03

(a)

(b)
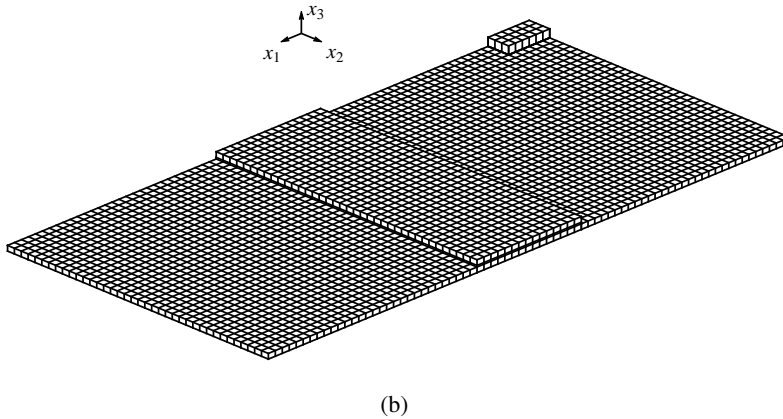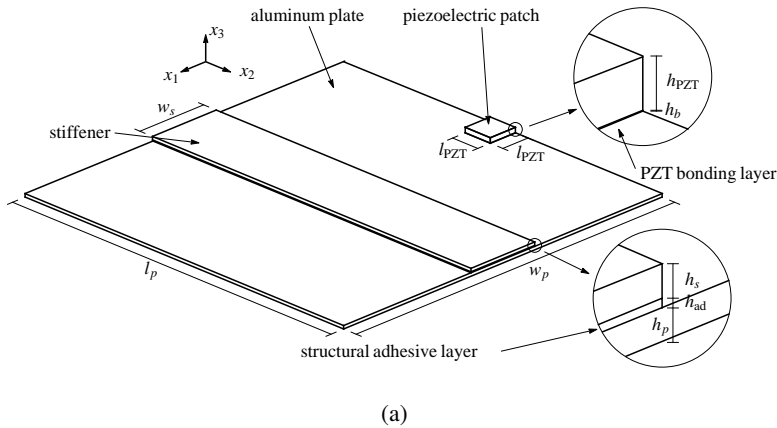
Figure 5: Numerical model of a lightweight adhesively bonded system. (a) geometry of the PZT glued to an aluminum plate stiffened with an adhesively bonded aluminum strip. (b) system mesh considered in the model. Mesh element size for the plate: 1.67 mm x 1.67 mm x 1.27 mm; mesh element size for the PZT: 1.67 mm x 1.67 mm x 2 mm; mesh element size for the bonding layer between the PZT and the plate: 1.67 mm x 1.67 mm x 0.03 mm; mesh element size for the bonding layer between the strip and the plate: 1.67 mm x 1.67 mm x 0.36 mm.

different properties of the structural adhesive in order to investigate the ability of the EMI technique to detect degradation in the quality of the adhesive layer. Two case studies were simulated: 1) different values of the Young modulus Y_{ad} at a given loss factor η_{ad}; 2) different values of η_{ad} and fixed Young modulus. The results relative to both cases are presented in Fig. 6, which shows the conductance as a
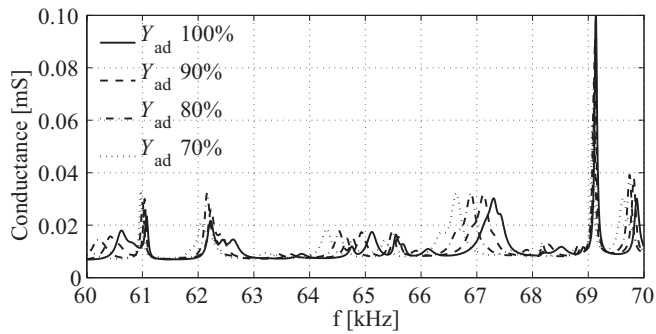
(a)
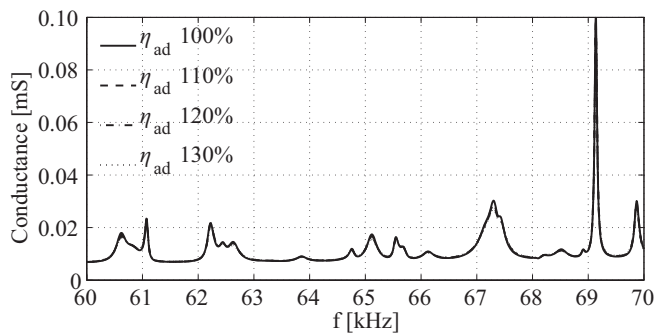
(b)
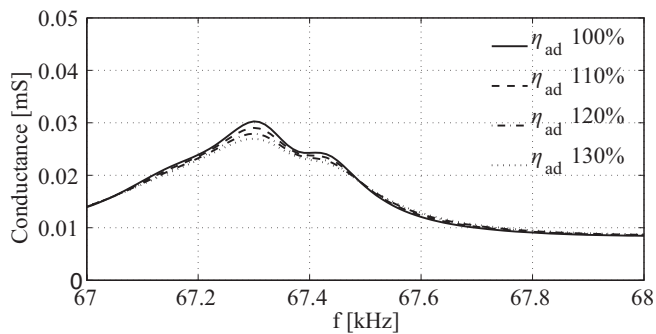
(c)

Figure 6: Conductance as a function of the excitation frequency at (a) different values of the Young modulus and at (b) different values of the loss factor of the bonding layer. (c) close-up view of the conductance as a function of the excitation frequency for four different values of the loss factor of the bonding layer.

function of the excitation frequency. The value $Y_{ad} = 100\%$ refers to an adhesive fully cured whereas lower values of the Young modulus indicate an adhesive that deteriorated. Figure 6a shows that the increase of the Young modulus causes a shift of peaks towards higher frequencies. This is expected since stiffness and resonance frequencies are directly proportional. On the other hand, the decrease of the loss factor induces a very small increase in the peaks' amplitude and makes the signature curve sharper, as shown in Fig. 6b and in the close-up view of Fig. 6c. This agrees with the fact that a less damped structure usually has higher peaks' amplitude. This small increase visible in Fig. 6c may be hardly noticeable when two experiments of the same setup will be run.

We did not reduce the Young modulus and did not increase the loss factor any further because the linear elastic model would not capture the viscous effects that prevail over the elastic effects during the early stage of curing.

5   EMI measurements

The measurement of the electrical impedance of a piezoelectric device is conventionally conducted using bulky equipment such as the HP 4192A or other commercial systems such as the Agilent E4980 LCR meter. A decade ago, Peairs et al. (2004) proposed to use a Fast Fourier Transform (FFT) analyzer and the inexpensive electrical circuit schematized in Fig. 7. The electrical impedanceZ_{PZT} was calculated dividing the voltage across the PZT by the current flowing through it. The authors showed that in the frequency domain, if the resistance R_S is small compared to Z_{PZT}, the electrical impedance can be approximated as:

$$Z_{PZT} = R_S \frac{V_i}{V_o} \tag{18}$$

where V_i and V_o are the Discrete Fourier Transforms (DFTs) of the voltage supplied to the circuit v_i and the voltage across the sensing resistor v_o, respectively. It is known [Peairs et al. (2004); Baptista and Filho (2009)] that the use of the simplified circuit: 1) provides an approximation of the actual impedance and the discrepancy increases with the increase of the excitation frequency; 2) requires an amplifier when the resistor R_S is very small; 3) necessitates a FFT analyzer. To measure external complex impedances, Analog Device developed an impedance converter system (AD5933 board) where the external impedance is excited by a known frequency, the response signal is sampled by an onboard analog-to-digital converter and a DFT is processed by an onboard digital signal processing engine. However, this device can be used up to 100 kHz, it can process up to 1024 samples, and the impedance range that can be measured depends on the value of the internal resistor [Overly et al. (2007); Park et al. (2007); Park et al. (2008); Na

et al. (2012)]. Baptista and Filho (2009) presented a method that, according to the authors, eliminates some of the previous drawbacks. The method uses a data acquisition (DAQ) connected to a PC and driven in LabView, and a resistor connected to the piezoelectric device used for EMI measurements.
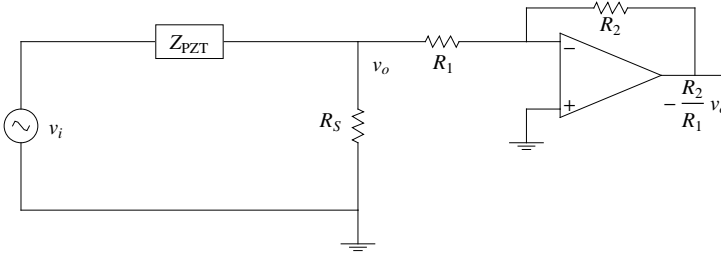
Figure 7: Circuit proposed by Peairs et al. (2004).

In our study we expanded the approach proposed by Baptista and Filho (2009). We connected an external auxiliary circuit to a National Instrument (NI) PXI running under LabView software, containing a function generator and a digitizer. The unknown impedance was calculated by measuring the frequency response of the circuit containing the impedance and an appropriate resistor. The whole system is schematized in Fig. 8a and its equivalent circuit is shown in Fig. 8b. The input signal was generated by a NI PXI-5421 Arbitrary Waveform Generator (AWG); the input and the output signals were acquired by a NI PXI-5122 digitizer, and controlled by a user-interface designed in house. We used a chirp signal to excite the circuit connected to the PZT. The signal can be analytically expressed as:

$$x_0[n] = A \sin \left[\frac{2\pi}{f_s} n \left(\frac{f_2 - f_1}{2N} n + f_1 \right) \right] \tag{19}$$

where f_s is the sampling frequency, N is the number of samples, A is the amplitude, and f_1 and f_2 are the start and the end frequency, respectively.

The digitizer sampled the analog input signal $x_1(t)$ and the analog output signal $x_2(t)$, and stored the corresponding digital input signal $x_1[n]$ and digital output signal $x_2[n]$. By using the FFT algorithm the DFTs $X_1[k]$ and $X_2[k]$ were calculated. These two complex arrays had N elements. The k-th element had a frequency equal to $(k-1)f_{res}$ where the frequency resolution f_{res} was equal to $f_{res} = f_s/N$. Finally, the frequency response function (FRF) $H[k]$ is computed by means of the cross power spectrum $S_{12}[k]$ and the auto power spectrum $S_{11}[k]$ as:

$$S_{12}[k] = X_1^*[k] X_2[k] \tag{20}$$

(a)

(b)
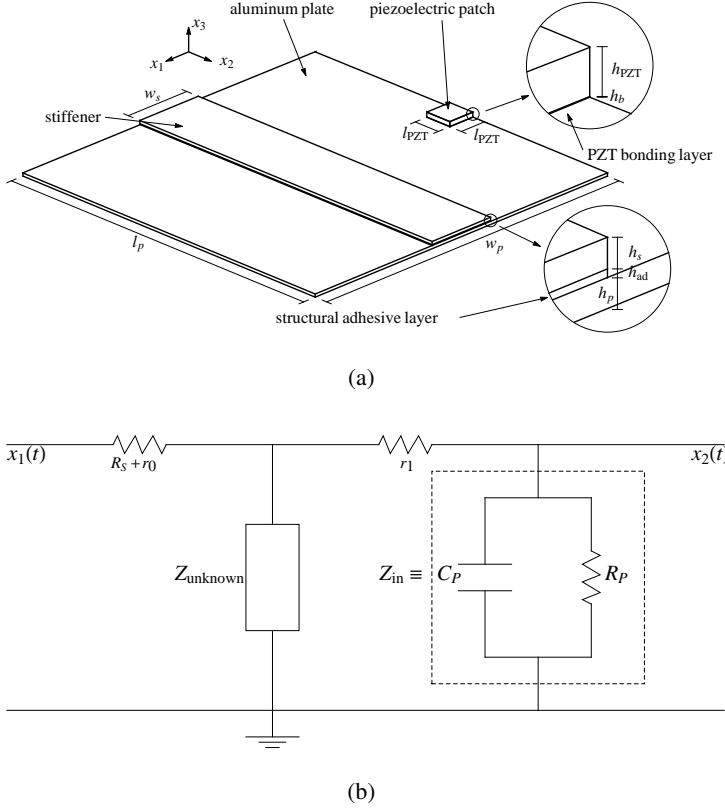
Figure 8: (a) scheme of the system used to measure the unknown impedance Z_{unknown} of a piezoelectric device. (b) equivalent circuit to the system shown in Fig. 8a. The FRF of the circuit is measured to calculate the unknown impedance Z_{unknown}.

$$S_{11}[k] = |X_1[k]|^2 \tag{21}$$

$$H[k] = \frac{S_{12}[k]}{S_{11}[k]} \tag{22}$$

where $X_1^*[k]$ is the complex conjugate of $X_1[k]$. In order to mitigate the effect of the noise and to obtain a more accurate FRF compared to a single measurement, an average of the FRF $H[k]$ was calculated as follows: given the value of the averaged $\bar{H}_{(i-1)}[k]$ at the $(i-1)$-th measurement, the value of the average $\bar{H}_{(i)}[k]$ at the i-th measurement was given by

$$\bar{H}_{(i)}[k] = \frac{\bar{H}_{(i-1)}[k] \cdot (i-1) + H_{(i)}[k]}{i} \tag{23}$$

where $H_{(i)}[k]$ is the FRF at the *i*-th measurement. In this way, it was not necessary to store all the measurements in order to calculate the average.

The relationship between the transfer function $H[k]$ and the unknown impedance $Z_{unknown}$ was obtained by using the equivalent circuit shown in Fig. 8b. In the circuit $x_1(t)$ and $x_2(t)$ represent the voltages measured by the digitizer; R_S is the resistor that controls the voltage across the unknown impedance $Z_{unknown}$ chosen such that the maximum voltage does not exceed the linear range of the PZT; r_0 and r_1 are the resistances of the cables connected to the auxiliary circuit; Z_{in} is the internal impedance of the DAQ device and consists of a resistance R_P in parallel with a capacitance C_P. Since the input signal was acquired very close to the user-defined signal $x_0(t)$, we safely assumed that $x_0(t) \cong x_1(t)$, which implied that $X_0[k] = X_1[k]$. From the circuital scheme of Fig. 8b, the DFT $X_1[k]$ of the input signal and the DFT $X_2[k]$ of the output signal are related as follows

$$\frac{X_2[k]}{X_1[k]} = H[k] = \frac{Z_{in}[k]Z_{unknown}[k]}{(R_S + r_0)(r_1 + Z_{in}[k]) + Z_{unknown}[k](R_S + r_0 + r_1 + Z_{in}[k])} \quad (24)$$

Equation (24) is solved for the unknown impedance $Z_{unknown}$

$$Z_{unknown}[k] = H[k] = \frac{\bar{H}[k](Z_{in}[k] + r_1)(R_S + r_0)}{Z_{in}[k] - \bar{H}[k](R_S + r_0 + r_1 + Z_{in}[k])} \quad (25)$$

The unknown impedance $Z_{unknown}$ was then calculated with Eq. 25 where $H[k]$ was replaced with $\bar{H}[k]$ that is the FRF measured and averaged with the system developed in this study. The electrical impedance $Z_{unknown}$ was obtained as a complex number consisting of the real part, the resistance $R_{unknown}$, and the imaginary part, the reactance $X_{unknown}$. In Eqs. 24 and 25, Z_{in} is the internal impedance that has the following expression

$$Z_{in}[k] = \left(\frac{1}{R_P} + j2\pi k f_{res} C_P \right)^{-1} \quad (26)$$

Finally, we computed the electrical admittance Y as the inverse of the $Z_{unknown}$ calculated with Eq. 25.

6   Experimental results

First, we bonded a 10 mm x 10 mm x 2 mm PSI 5A4E transducer, manufactured by PiezoSystem to the center of one edge of a 127 mm x 127 mm x 1.27 mm aluminum plate. Free boundary conditions were reproduced by placing the plate on a soft plastic layer. The unknown impedance is now the PZT patch bonded to the host structure and it depends on the patch-structure interaction. The conductance and

the susceptance of the system are presented in Figs. 9a and 9b, respectively. The graphs are overlapped to the case of the free PZT. Since the PZT does not resonate within this range, the peaks are relative to the modes of vibration of the structure. A close-up view of the range 60-70 kHz is presented in Figs. 9c and 9d. This range still contains a considerable number of peaks and is far enough from the natural modes of vibration of the PZT.
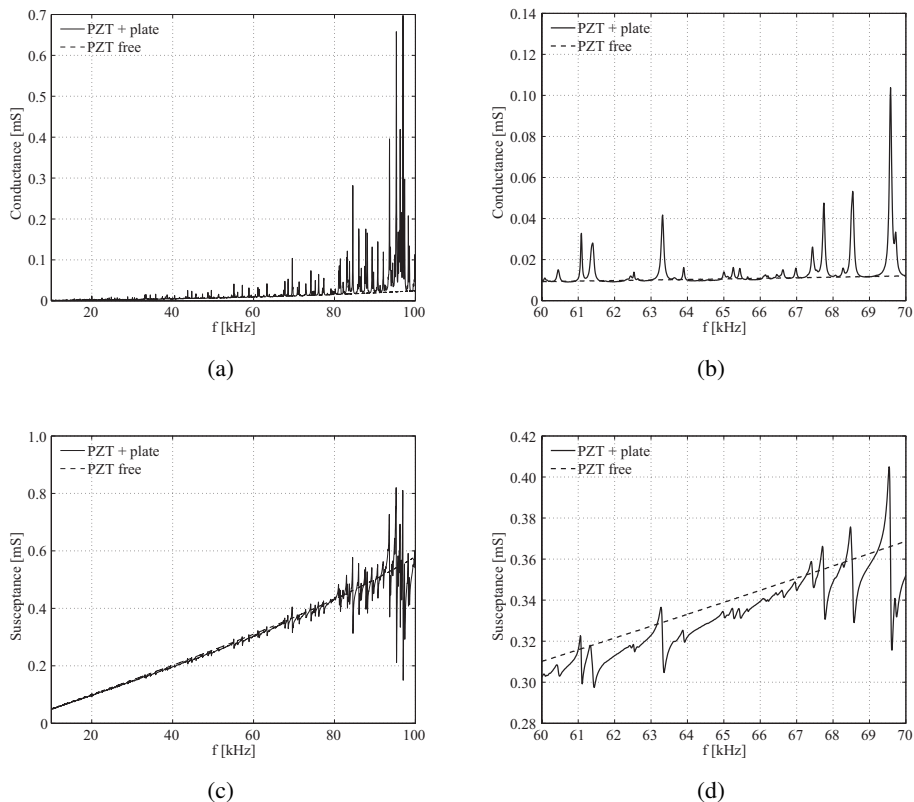
Figure 9: (a) conductance and (b) susceptance signatures of the free piezoelectric patch and of the same patch bonded to the aluminum plate. Close-up view in the frequency range 60-70 kHz of (c) the conductance and (d) the susceptance signatures of the free piezoelectric patch and the piezoelectric patch bonded to the structure.

Then, a few experiments were conducted to prove the feasibility of the EMI method to monitor adhesively-bonded joints. The same plate described above was stiffened with an aluminum strip bonded to a plate, as shown in Fig. 10. We prepped the

surface of the plate and the stiffener according to the recommendations of the adhe-sive's manufacturer; the surfaces were abraded by means of sand paper to increase the bonding surface. The structural adhesive was a commercial Devcon 2 Ton Epoxy type. Soon after the placement of the stiffener above the plate, we mea-sured the electromechanical response of the PZT every 10 minutes for 12 hours. Figure 11 presents the results associated with two frequency ranges: 10 – 80 kHz which contains all the resonance peaks of the host structure below the natural fre-quencies of the PZT patch; 60 – 70 kHz which is representative of the behavior of the conductance with respect to different modulus' values of the adhesive and with respect to which the numerical results are compared. Figure 11a shows the conductance as a function of the excitation frequency relative to three different in-stants, namely the first (the baseline) and the last measurements, and after 6 h. The narrower range 60-70 kHz is shown in Fig. 11b. The signature varied significantly with time, especially within the first six hours. Between t = 6 h and t = 11 h 50 min the response did not change significantly in shape but rather shifts horizontally and becomes sharper. In particular, many peaks seem to increase in amplitude and to move towards higher frequencies. This is due to the increase of the Young modulus and the decrease of the damping characteristics of the adhesive.
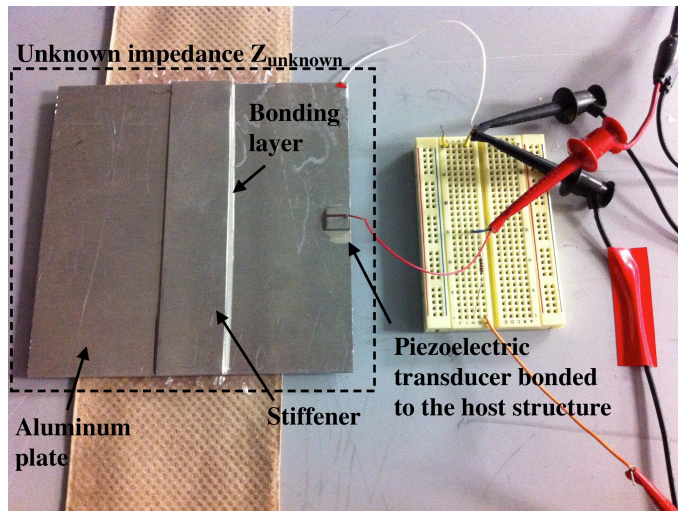
Figure 10: Auxiliary circuit where the PZT transducer is bonded to the aluminum plate with the stiffener.

Figure 12 shows a waterfall plot containing the conductance measured during the experiment. We want to emphasize that the curing process can be considered at large the inverse of the degradation process. All the ridges visible in this waterfall
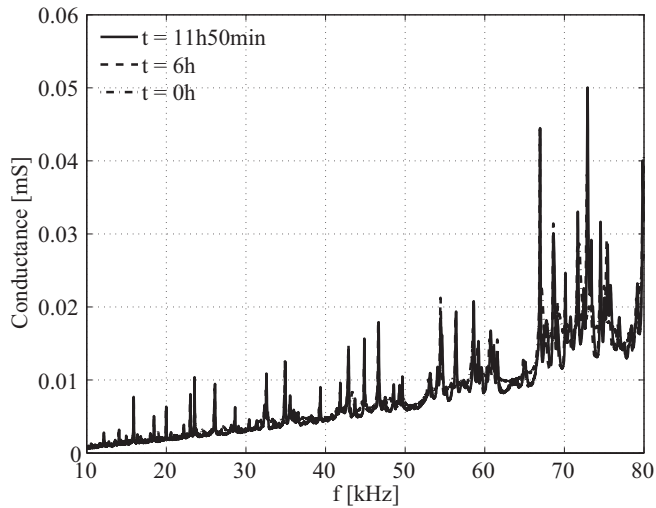
(a)
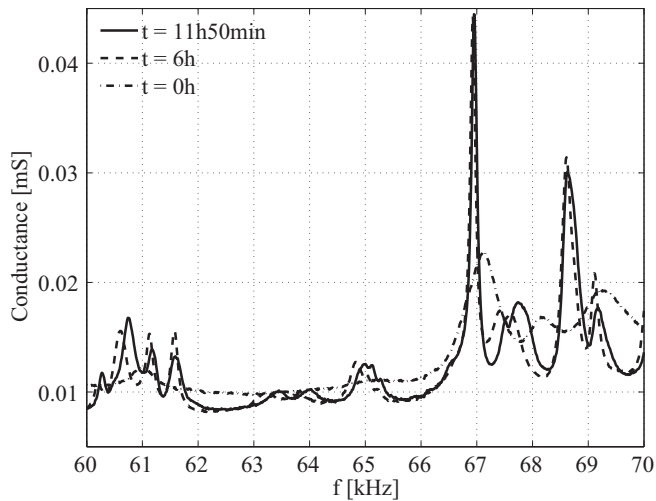
(b)

Figure 11: Conductance signature of the PZT bonded to the aluminum plate with the stiffener at t = 0 h, t = 6 h and t = 11 h 50 min. (a) frequency range from 10 kHz to 80 kHz. (b) closeup view in the range 60-70 kHz.
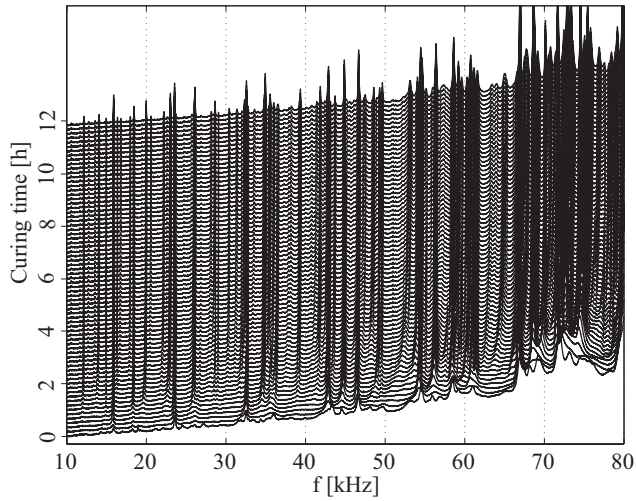
(a)
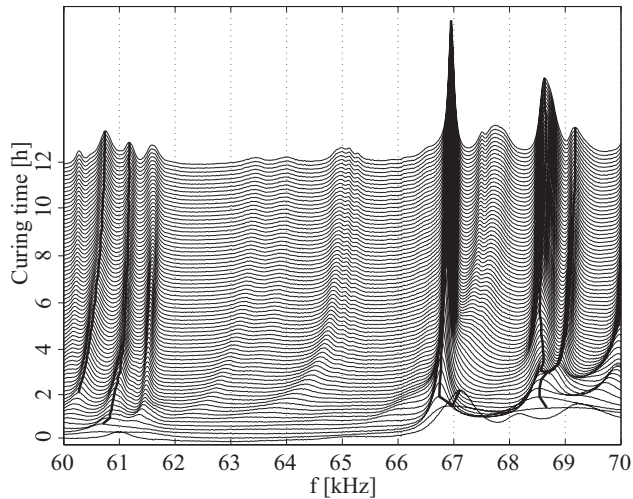
(b)

Figure 12: Variation with time of the conductance signature of the PZT bonded to the aluminum plate with the stiffener. (a) frequency range from 10 kHz to 80 kHz. (b) closeup view in the range 60-70 kHz.
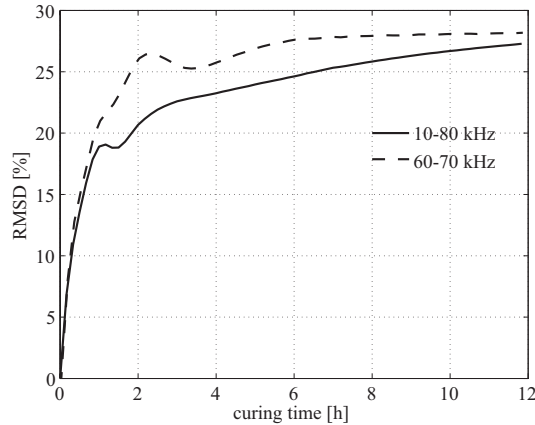
Figure 13: RMSD as a function of time during the curing time. RMSD calculated for two frequency ranges: (solid line) 10-80 kHz, (dashed line) 60-70 kHz.

plot show a significant increase toward higher frequencies. This shift is particularly evident within the first five hours. In the last seven hours of curing, the shape basically remains unchanged whereas the frequencies and the amplitudes of the peaks change. This is clearly visible in the close-up view presented in Fig. 12b which shows the development of the ridges relative to five structural peaks. New peaks are visible after 2-3 hours and then steadily increase in amplitude. This means that as the adhesive cures, the stiffened plate develops more vibration modes which translate into more peaks in the conductance signature. We note that the variation of the ridges' frequency is less than 1 kHz, which means that the measurement system needs to possess sufficient resolution in order to capture the variations of the bond quality.

In the EMI technique the assessment of damage is sometimes carried out by means of statistical indices. In the present study we considered the Root Mean Square Deviation (RMSD) [Soh et al. (2000); Giurgiutiu and Rogers (1998); Giurgiutiu et al. (1999)], defined as

$$RMSD(\%) = \sqrt{\frac{\sum\limits_{i=1}^{N} \left(G_i^k - G_i^1\right)^2}{\sum\limits_{i=1}^{N} \left(G_i^1\right)^2}} \cdot 100 \tag{27}$$

where G_i^k and G_i^1 are the i-th data-sample of the conductance associated with the k-th measurement and the baseline measurement, respectively; N is the number

of frequency points considered. In this study the baseline is represented by the measurement at t = 0 h. Figure 13 shows the RMSD as a function of the curing time for the two frequency ranges considered. Clearly, in the first four hours of curing, there was the largest change in the value of the index; after that, the index changed less and tended to reach a constant value. It is worth noting that the behavior of the curves and the final percentile variations are similar, irrespective of the frequency range considered. As such, the 60-70 kHz range can be used as representative of the wider 10-80 kHz range.

7   Comparison between numerical and experimental results

In order to carry out a comparative study between the numerical model and the experimental results, we considered the free PZT, first. Figures 14a and 14b show respectively the numerical and the experimental conductance and susceptance signatures. There is a very good agreement between measured and computed data. The slight discrepancy at 436 kHz vs 431 kHz may be due to the fact that not all the parameters of the constitutive matrices used in the finite element model were available the manufacturer.

We then compared the PZT-plate interaction and the results are presented in Fig. 15, again in terms of the conductance and the susceptance. The agreement between numerical and experimental results is not as good as for the free PZT since the numerical results present peaks with higher amplitude. This may be attributable to one or more of the following factors: 1) the numerical analysis was computed under free boundary conditions; in the experiments the plate laid on a bench table; in the future this issue can be easily solved by hanging the test object from the roof, for example. 2) the size and the thickness of the glue may not be the same and difficult to control. 3) the actual strength of the glue may not be the same as hypothesized in the FEM simulation. Nonetheless, the number and the distribution of the peaks and the general behavior of the two curves match.

Finally, the numerical and the experimental results relative to the adhesive joint are compared. Figure 16 displays the numerical result presented in Fig. 9a associated with the fully cured specimen (Y_{ad}=100%) overlapped to the experimental data. Similar to the previous case, the numerical response shows a sharper signature whereas the position and the number of the peaks agree. In order to compare the numerical and the experimental progression of the bond quality, Fig. 17 is presented. Figure 17a shows the experimental conductance at t = 6 h, 8 h, 10 h, 11 h 50 min. The response is shown only for the last 6 hours since we believe that the linear elastic model cannot model fresh adhesive appropriately, i.e. depict the early stage of curing. While curing, the adhesive of the joint becomes stiffer and less viscous and this is visible in the behavior of the peaks that occur at higher frequencies
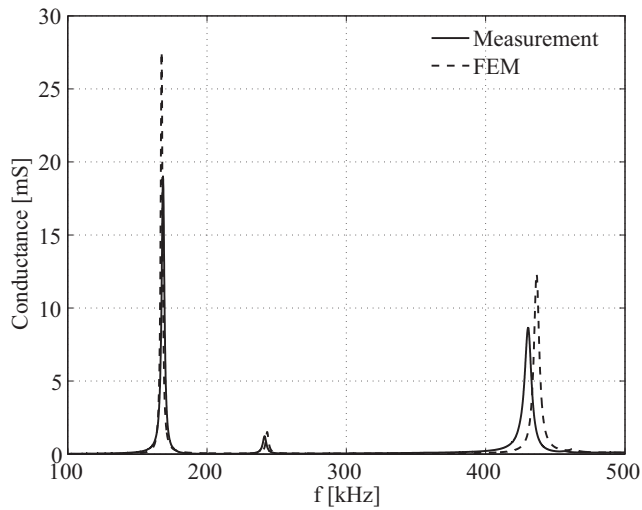
(a)
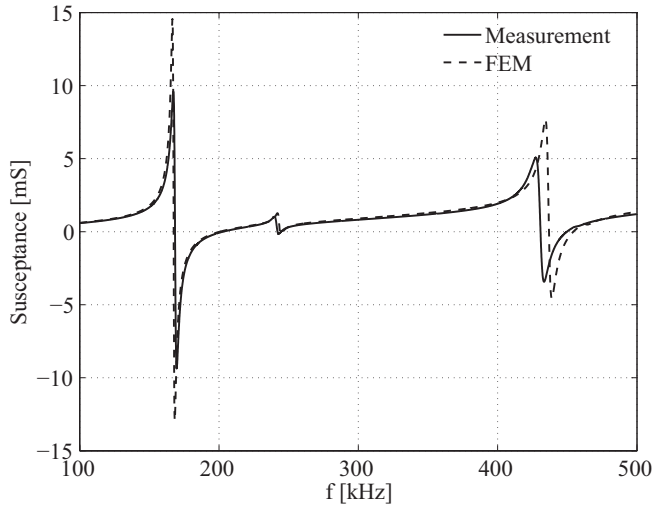
(b)

Figure 14: Comparison between experimental and numerical results for the (a) conductance signature and the (b) susceptance signature of the free PZT.
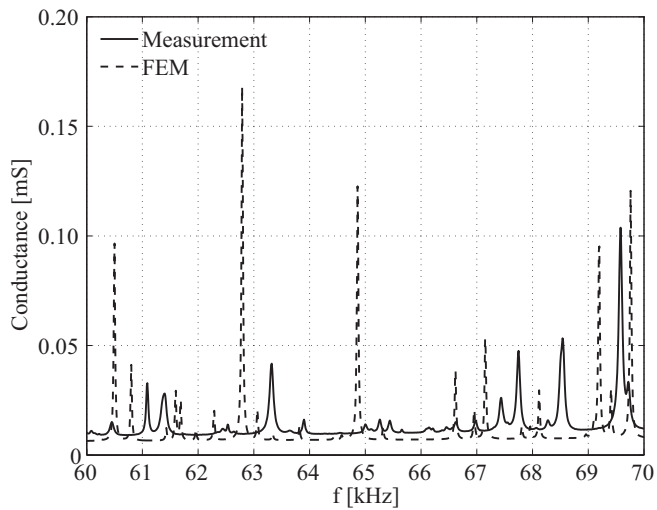
(a)
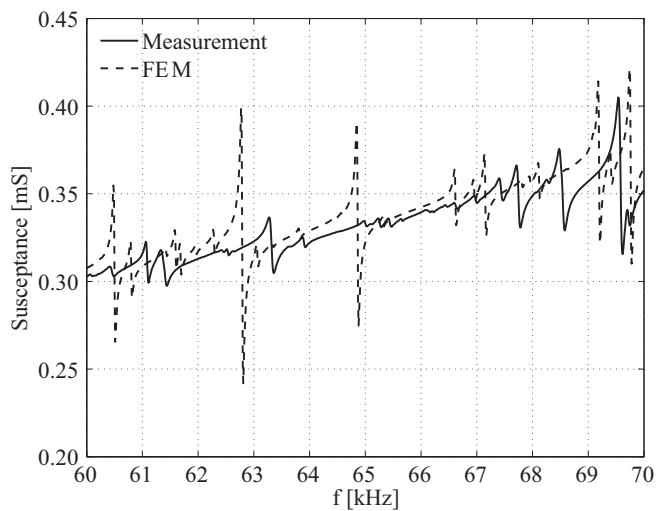
(b)

Figure 15: Comparison between experimental and numerical results for the (a) conductance signature and the (b) susceptance signature of the PZT bonded to the plate.
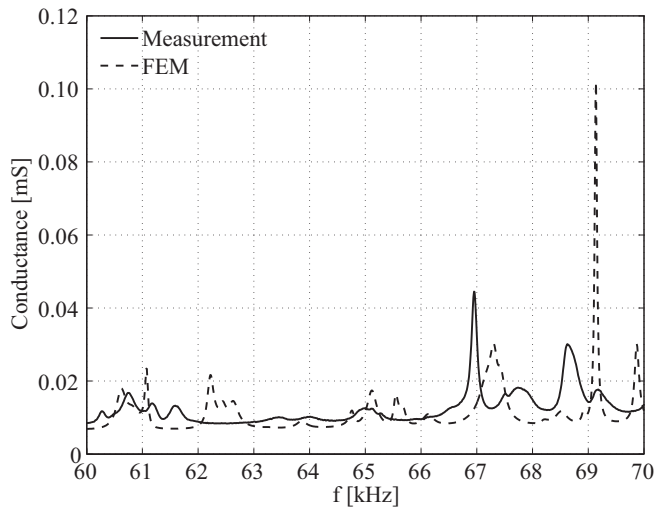
(a)
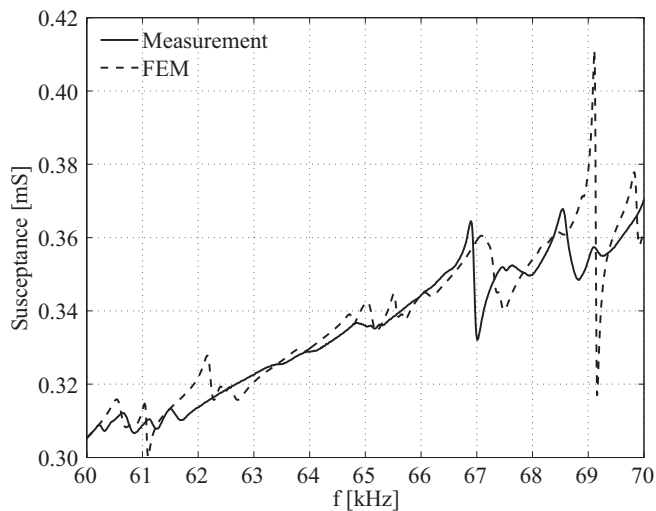
(b)

Figure 16: Comparison between experimental and numerical results for the (a) conductance signature and the (b) susceptance signature of the PZT bonded to aluminum plate with the stiffener at the end of the curing.
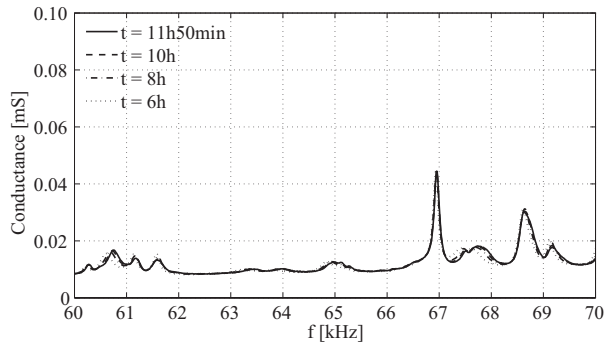
(a)
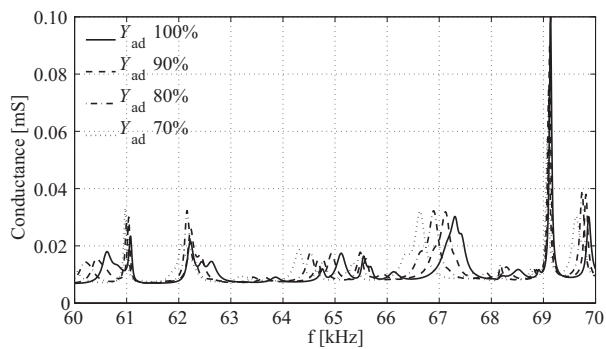
(b)
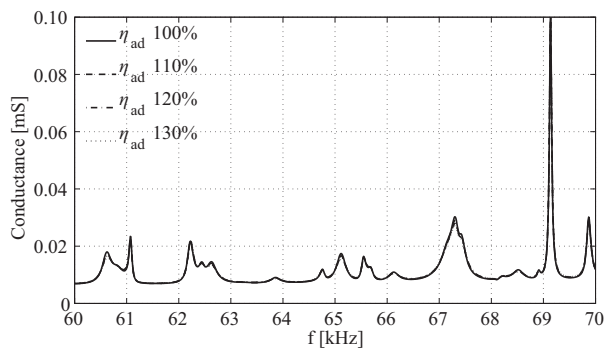
(c)

Figure 17: Conductance as a function of the actuation frequency: (a) experimental results associated with four instants of curing, namely at t = 6 h, 8 h, 10 h, 11 h 50 min. (b) numerical results associated with four values of the adhesive's Young modulus. (c) numerical results associated with four values of the adhesive's loss factor.
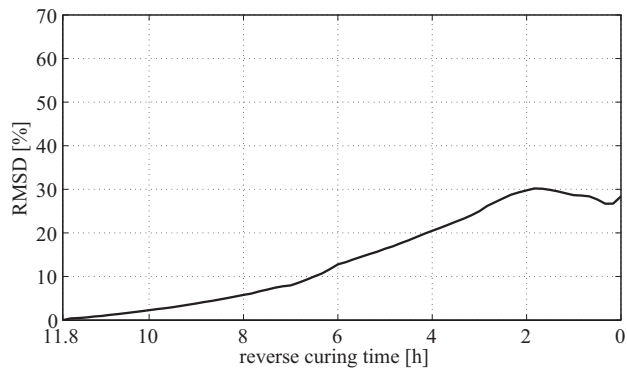
(a)
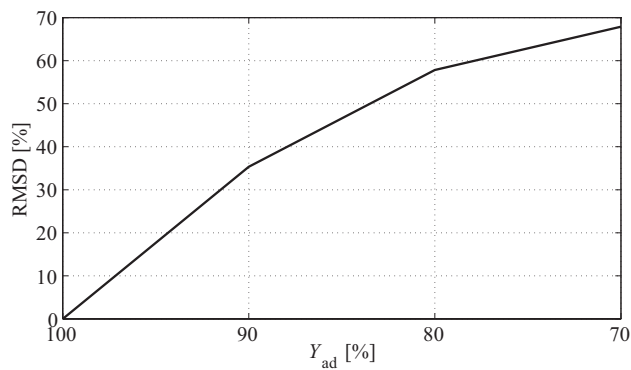
(b)
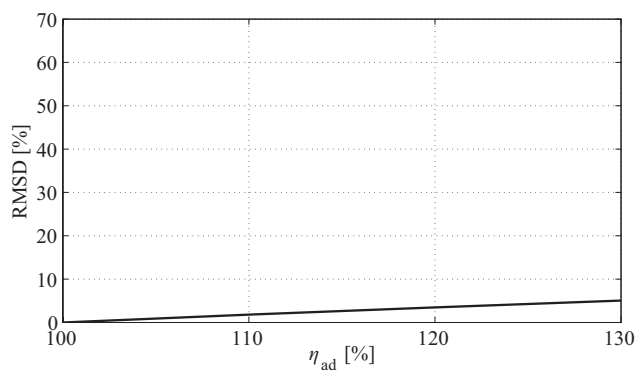
(c)

Figure 18: Comparison between (a) the value of the RMSD index calculated using the last measurement of the curing as the baseline, and the value of the RMSD index as function of the (b) Young modulus and (c) loss factor of the adhesive.

and increase their amplitude. Figure 17b shows the conductance as a function of the excitation frequency predicted numerically when the loss factor is kept constant and the Young' modulus deteriorates. Similarly, Fig. 17c shows the numerical prediction of the conductance when the loss factor changes and the Young's modulus remains constant. In accordance with the experimental results, we note that the increase of the Young modulus at a given loss factor tends to shift the modes of structural vibration towards higher frequencies. On the other hand, the decrease of the loss factor at a given Young modulus tends to sharp the signature.

Finally, Figure 18 shows how the RMSD may be employed as an index of the degradation of the joint. Figure 18a shows the index as a function of the reverse curing time, and it was calculated by considering the last measurement as baseline. The instants at the beginning of the curing may depict at large a poor joint. Figures 18b and 18c show the RMSD index calculated for the decreasing value of the Young modulus and the increasing value of the loss factor, respectively. As one may notice, a 30% variation in the Young modulus leads to a much higher value of the RMSD with respect to the same percentile variation of the loss factor. The disagreement between the numerical and the experimental results have already been discussed above. Nonetheless, we can conclude that the trend and the behavior of the signature with respect to different properties of the bonded joint were captured.

8 Conclusions

In the study presented in this paper the electromechanical impedance (EMI) method is utilized to monitor an adhesively bonded system representative of a lightweight small component used in the aircraft industry. The structural health monitoring approach hypothesizes that a wafer-type lead zirconate titanate transducer attached to the structure to be monitored can assess the quality of the bond. In fact, when subjected to an electric field, the transducer induces structural excitations which, in turn, affect the transducers electrical admittance. As the structural vibrations depend on the strength of the bond, the measurement of the transducer's admittance can be exploited to assess the quality of the bond itself. Overall, the proposed methodology has the advantage of any EMI-based structural health monitoring strategy: low cost and sensitivity to material changes in a localized area around the sensors.

A finite element model was first implemented to predict the admittance of the transducer employed to monitor joints subjected to varying conditions of the adhesive layer. To the best of our knowledge, this is the first time that an ad hoc finite element model implemented to predict the electromechanical coupling between a wafer-type transducer and a host structure. In fact, previous researchers have used commercial software to model the EMI method. The model was then verified by

a series of experiments aimed at monitoring the curing progress of an adhesive layer between an aluminum plate and an aluminum strip. The bond was realized by means of a commercial two-part epoxy and the curing process was monitored for about 12 hours. The results demonstrated that as the curing progresses, the characteristics of the electrical conductance change. The experimental results were also interpreted by comparing them to the numerical results obtained with the finite element model. We found that most of the experimental and the numerical results are in good agreement with each other; any discrepancy is likely related to the boundary conditions and the exact knowledge of the size, thickness, and strength of the adhesive layers used to glue the PZT and to bond the stiffener to the plate.

An ongoing study is evaluating the repeatability of the methodology by considering a large pool of samples. Future studies shall instead consider the effect of the temperature on this specific application.

References

Allik, H.; Hughes, T. J. (1970): Finite element method for piezoelectric vibration. *International journal for numerical methods in engineering*, vol. 2, no. 2, pp. 151-157.

Allik, H.; Webman, K. M.; Hunt, J. T. (1974): Vibrational response of sonar transducers using piezoelectric finite elements. *The Journal of the Acoustical Society of America*, vol. 56, pp. 1782-1791.

Annamdas, V. G. M.; Soh, C. K. (2007): Three-dimensional electromechanical impedance model. I: Formulation of directional sum impedance. *Journal of Aerospace Engineering*, vol. 20, no. 1, pp. 53-62.

Ayres, J. W.; Lalande, F.; Chaudhry, Z.; Rogers, C. A. (1998): Qualitative impedance-based health monitoring of civil infrastructures. *Smart Materials and Structures*, vol. 7, no. 5, pp. 599-605.

Baker, A. A.; Jones, R. (1988): *Bonded repair of aircraft structures*. Springer.

Baker, A. A.; Rose, L. F.; Jones, R. (2003): *Advances in the bonded composite*

repair of metallic aircraft structure. Elsevier.

Baptista, F. G.; Filho, J. V. (2009): A new impedance measurement system for PZT-based structural health monitoring. *Instrumentation and Measurement, IEEE Transactions on*, vol. 58, no. 10, pp. 3602-3608.

Bathe, K.-J. (1996): *Finite element procedures*. Prentice hall Englewood Cliffs.

Bhalla, S; Soh, C. K. (2004): Electromechanical impedance modeling for adhesively bonded piezotransducers. *Journal of Intelligent Material Systems and Structures*, vol. 15, no. 12, pp. 955-972.

Bhalla, S; Soh, C. K. (2012): Electro-Mechanical Impedance Technique. *Smart Materials in Structural Health Monitoring, Control and Biomechanics*, Springer, pp. 17-51.

Bhalla, S.; Yang, Y.; Annamdas, V.; Lim, Y.; and Soh, C. (2012): Impedance Models for Structural Health Monitoring Using Piezo-Impedance Transducers. *Smart Materials in Structural Health Monitoring, Control and Biomechanics*, Springer, pp. 53-128.

Chen, L.; Zhang, Y. W.; Liu, G. R.; Nguyen-Xuan, H.; Zhang, Z. Q. (2012): A stabilized finite element method for certified solution with bounds in static and frequency analyses of piezoelectric structures. *Computer Methods in Applied Mechanics and Engineering*, vol. 241-244, no. 6, pp. 65-81.

Crawley, E. F. (1994): Intelligent structures for aerospace-A technology overview and assessment. *AIAA journal*, vol. 32, no. 8, pp. 1689-1699.

Crawley, E. F.; De Luis, J. (1987): Use of piezoelectric actuators as elements of intelligent structures. *AIAA journal*, vol. 25, no. 10, pp. 1373-1385.

Giurgiutiu, V.; Reynolds, A.; Rogers, C. A. (1999): Experimental investigation of E/M impedance health monitoring for spot-welded structural joints. *Journal of Intelligent Material Systems and Structures*, vol. 10, no. 10, pp. 802-812.

Giurgiutiu, V.; Rogers, C. A. (1998): Recent advancements in the electro-mechanical (ElM) impedance method for structural health monitoring and NDE. *SPIE 5th International Symposium on Smart Structures and Materials*, pp. 1-5.

Giurgiutiu, V.; Zagrai, A. N. (2002): Embedded self-sensing piezoelectric active sensors for on-line structural identification. *Transactions-American Society of Mechanical Engineers Journal of Vibration and Acoustics*, vol. 124, no. 1, pp. 116-125.

Guyott, C. H.; Cawley, P. (1988): The ultrasonic vibration characteristics of adhesive joints. *The Journal of the Acoustical Society of America*, vol. 83, no. 2, pp. 632-640.

Guyott, C. H.; Cawley, P.; Adams, R. (1986): The non-destructive testing of

adhesively bonded structure: a review. *The Journal of Adhesion*, vol. 20, no. 2, pp. 129-159.

Higgins, A. (2000): Adhesive bonding of aircraft structures. *International Journal of Adhesion and Adhesives*, vol. 20, no. 5, pp. 367-376.

Lanza di Scalea, F.; Rizzo, P.; Marzani, A. (2004): Assessment of Bond State in Lap-Shear Joints by Guided Wave Transmission Monitoring. *Insight-Non- Destructive Testing & Condition Monitoring*, vol. 46, no. 3, pp. 135-141.

Lanza di Scalea, F.; Rizzo, P.; Marzani, A. (2004): Propagation of Ultrasonic Guided Waves in Lap-shear Adhesive Joints: case of Incident a0 Lamb Wave. *The Journal of the Acoustical Society of America*, vol. 115, no. 1, pp. 146-156.

Lerch, R. (1990): Simulation of piezoelectric devices by two-and three-dimensional finite elements. *Ultrasonics, Ferroelectrics and Frequency Control, IEEE Transactions on*, vol. 37, no. 3, pp. 233-247.

Liang, C.; Sun, F.; Rogers, C. (1994): An impedance method for dynamic analysis of active material systems. *Journal of Vibration and Acoustics*, vol. 116, no. 1, pp. 120-128.

Liu, W.; Giurgiutiu, V. (2007): Finite element simulation of piezoelectric wafer active sensors for structural health monitoring with coupled-field elements. *The 14th International Symposium on: Smart Structures and Materials & Nondestructive Evaluation and Health Monitoring*, International Society for Optics and Photonics, pp. 65293R-65293R.

Lowe, M.; Challis, R.; Chan, C. (2000): The transmission of Lamb waves across adhesively bonded lap joints. *The Journal of the Acoustical Society of America*, vol. 107, pp. 1333-1345.

Makkonen, T.; Holappa, A.; Ella, J.; Salomea, M. (2001): Finite element simulations of thin-film composite BAW resonators. *Ultrasonics, Ferroelectrics and Frequency Control, IEEE Transactions on*, vol. 48, no. 5, pp. 1241-1258.

Malinowski, P. H.; Wandowski, T.; Ostachowicz, W. M. (2014): Characterisation of CFRP adhesive bonds by electromechanical impedance. *SPIE Smart Structures and Materials+Nondestructive Evaluation and Health Monitoring*, International Society for Optics and Photonics, pp. 906415-906415.

Matt, H.; Bartoli, I.; Lanza di Scalea, F. (2005): Ultrasonic guided wave monitoring of composite wing skin-to-spar bonded joints in aerospace structures. *The Journal of the Acoustical Society of America*, vol. 118, no. 4, pp. 2240-2252.

Mezheritsky, A. V. (2004): Elastic, dielectric, and piezoelectric losses in piezoceramics: how it works all together. *Ultrasonics, Ferroelectrics and Frequency Control, IEEE Transactions on*, vol. 51, no. 6, pp. 695-707.

Moharana, S.; Bhalla, S. (2012): Numerical investigations of shear lag effect on PZT-structure interaction: review and application. *Current Science*, vol. 103, no. 6, pp. 685-696.

Na, S.; Tawie, R.; Lee, H. K. (2012): Electromechanical impedance method of fiber-reinforced plastic adhesive joints in corrosive environment using a reusable piezoelectric device. *Journal of Intelligent Material Systems and Structures*, vol. 23, no. 7, pp. 737-747.

Nagy, P. B. (1991): Ultrasonic detection of kissing bonds at adhesive interfaces. *Journal of Adhesion Science and Technology*, vol. 5, no. 8, pp. 619-630.

Nagy, P. B. (1992): Ultrasonic classification of imperfect interfaces. *Journal of Nondestructive evaluation*, vol. 11, no. 3-4, pp. 127-139.

Overly, T. G.; Park, G.; Farrar, C. R.; Allemang, R. J. (2007): Compact hardware development for SHM and sensor diagnostics using admittance measurements. *SEM International Modal Analysis Conference*.

Park, S.; Ahmad, S.; Yun, C. B.; Roh, Y. (2006): Multiple crack detection of concrete structures using impedance-based structural health monitoring techniques. *Experimental Mechanics*, vol. 46, no. 5, pp. 609-618.

Park, G.; Cudney, H. H.; and Inman, D. J. (2001): Feasibility of using impedance-based damage assessment for pipeline structures. *Earthquake engineering & structural dynamics*, vol. 30, no. 10, pp. 1463-1474.

Park, S.; Lee, J.-J.; Yun, C.-B.; Inman, D. J. (2007): A built-in active sensing system-based structural health monitoring technique using statistical pattern recognition. *Journal of mechanical science and technology*, vol. 21, no. 6, pp. 896-902.

Park, S.; Lee, J.-J.; Yun, C.-B.; Inman, D. J. (2008): Electro-mechanical impedance-based wireless structural health monitoring using PCA-data compression and k-means clustering algorithms. *Journal of Intelligent Material Systems and Structures*, vol. 19, no. 4, pp. 509-520.

Park, G.; Sohn, H.; Farrar, C. R.; Inman, D. J. (2003): Overview of piezoelectric impedance-based health monitoring and path forward. *Shock and Vibration Digest*, vol. 35, no. 6, pp. 451-464.

Peairs, D. M., Park, G., Inman, D. J. (2004): Improving accessibility of the impedance-based structural health monitoring method. *Journal of Intelligent Material Systems and Structures*, vol. 15, no. 2, pp. 129-139.

Rothenfusser, M.; Mayr, M.; Baumann, J. (2000): Acoustic nonlinearities in adhesive joints. *Ultrasonics*, vol. 38, no. 1, pp. 322-326.

Schroeder, J., Ahmed, T.; Chaudhry, B.; Shepard, S. (2002): Non-destructive testing of structural composites and adhesively bonded composite joints: pulsed

thermography. *Composites Part A: Applied Science and Manufacturing*, vol. 33, no. 11, pp. 1511-1517.

Soh, C., Tseng, K. K., Bhalla, S., Gupta, A. (2000): Performance of smart piezoceramic patches in health monitoring of a RC bridge. *Smart materials and Structures*, vol. 9, no. 4, pp. 533-542.

Sun, F. P.; Chaudhry, Z. A.; Rogers, C. A.; Majmundar, M., Liang, C. (1995): Automated real-time structure health monitoring via signature pattern recognition. *Proc. SPIE Smart Structures and Materials 1995: Smart Structures and Integrated Systems*, vol. 2443.

Tabrizi, A.; Rizzo, P.; and Ochs, M. W. (2012): Electromechanical impedance method to assess dental implant stability. *Smart Materials and Structures*, vol. 21, no. 11, pp. 115022.

Tawie, R.; Lee, H. K. (2010): Piezoelectric-based non-destructive monitoring of hydration of reinforced concrete as an indicator of bond development at the steel–concrete interface. *Cement and Concrete Research*, vol. 40, no. 12, pp. 1697-1703.

Tiersten, H. (1967): Hamilton's principle for linear piezoelectric media. *Proceedings of the IEEE*, vol. 55, no. 8, pp. 1523-1524.

Todd, M.; Lanza di Scalea, F.; Srivastava, A.; Fasel, T.; Bartoli, I. (2010): In-Situ Adhesive Bond Assessment. *Univ. of California, San Diego, Final Report*, AFRL-SA-AR-TR-10-0344.

Vijaya Kumar, R.; Bhat, M.; Murthy, C. (2013): Evaluation of kissing bond in composite adhesive lap joints using digital image correlation: Preliminary studies. *International Journal of Adhesion and Adhesives*, vol. 42, pp. 60-68.

Waugh, R.; Dulieu-Barton, J. M.; Quinn, S. (2011): Pulse phase thermography and its application to kissing defects in adhesively bonded joints. *Applied Mechanics and Materials*, vol. 70, pp. 369-374.

Yan, D.; Drinkwater, B. W.; Neild, S. A. (2009): Measurement of the ultrasonic nonlinearity of kissing bonds in adhesive joints. *Ndt & E International*, vol. 42, no. 5, pp. 459-466.

Zhang, Y.; Xu, F.; Chen, J.; Wu, C.; Wen, D. (2011): Electromechanical impedance response of a cracked timoshenko beam. *Sensors*, vol. 11, no. 7, pp. 7285-7301.

Zhou, S.; Liang, C.; Rogers, C. (1995): Integration and design of piezoceramic elements in intelligent structures. *Journal of Intelligent Material Systems and Structures*, vol. 6, no. 6, pp. 733-743.